PHYSICAL REVIEW B VOLUME 49, NUMBER 22 1 JUNE 1994-II

Spectroscopy and dynamics of Cr^{4+}:$Y_3Al_5O_{12}$

Hergen Eilers, Uwe Hömmerich, Stuart M. Jacobsen, and William M. Yen
Department of Physics, University of Georgia, Athens, Georgia 30602

K. R. Hoffman
Department of Physics, Whitman College, Walla Walla, Washington 99362

W. Jia
Department of Physics, University of Puerto Rico, Mayaguez, Puerto Rico 00680

(Received 19 May 1993; revised manuscript received 27 October 1993)

We present a spectroscopic overview of Cr^{4+}-doped $Y_3Al_5O_{12}$ (YAG), a new laser material for the near-infrared region (NIR). It is found that only 2% of the Cr ions are tetrahedrally coordinated Cr^{4+}. However, the optical spectra are dominated by this ion. The missing inversion symmetry for the tetrahedral site causes higher cross sections than are common for octahedrally coordinated ions. The experimental data include a survey of the absorption and emission features. Lifetime measurements, as well as piezospectroscopic experiments yield additional spectroscopic information. Our data suggest an energy-level assignment that is different from the one previously used to describe the spectrum. Instead of ascribing the strong NIR absorption band, centered at around 1000 nm, to the ${}^3B_1({}^3A_2) \Longrightarrow {}^3E({}^3T_2)$ transition, we assign it to the ${}^3B_1({}^3A_2) \Longrightarrow {}^3A_2({}^3T_1)$ transition. This assignment is able to describe the polarization-dependent spectra, the piezospectroscopic results, and the results from earlier polarization-dependent saturation experiments. An analysis of the luminescence decay rate yields quantum efficiencies of around 49% at 10 K and 15% at room temperature, resulting in a peak emission cross section of 3.5×10^{-19} cm^2.

I. INTRODUCTION

Since the successful demonstration of Cr-doped Forsterite (Mg_2SiO_4) (Refs. 1 and 2) and Cr-doped YAG (Refs. 3–6) as near-infrared (NIR) tunable lasers there has been considerable interest in the spectroscopic properties of these materials. Under normal growing conditions Cr enters these materials as Cr^{3+} in octahedral sites. Because of the oxidizing growth condition and/or co-doping with charge compensators it is believed that, in the above-mentioned samples, tetrahedrally coordinated Cr^{4+} is responsible for the NIR emission. Meanwhile a lot of other materials, doped with Mn^{5+} and Fe^{6+} which are isoelectronic with Cr^{4+}, have been investigated. The spectroscopy of these d^2 systems is fairly well understood.[7–9] All samples that have been studied so far are high-field systems, i.e., the first excited state is a spin singlet while the ground state is a spin triplet. The NIR emission is characterized by sharp emission peaks with lifetimes of a few hundreds of μs. The relatively long lifetimes are expected for such spin-flip transitions.

The spectroscopic features of the Cr-doped systems differ from the Mn- and Fe-doped systems. The emission from the Cr ion is spectrally broader and has lifetimes in the range of a few tens of μs.[10–14] These features make it more likely that the Cr ion is a low-field system where the first excited state is a spin triplet as is the ground state. A transition between these two states would therefore be spin allowed and should show a shorter lifetime compared to the high-field case. For the low-field case the first excited state should be the ${}^3T_2$ state. For Cr-doped Forsterite it has been shown that the lowest orbital component of the first excited state is a spin triplet.[14] This fact supports the assignment of the first excited state as the ${}^3T_2$ state.

Most of the Cr-doped materials belong to a noncubic space group, with the Cr ion in a characteristic site symmetry and with a certain orientation with regard to the crystallographic axes. This fact makes it easy to take polarization-dependent spectra and assign energy levels with respect to group theory.

For Cr-doped YAG the spectroscopic investigation is not as simple. The problems arise from the following facts: YAG belongs to the garnet family with a cubic space group. The spectroscopic properties are therefore, in general, isotropic. Furthermore, YAG has to be codoped with Ca^{2+} or Mg^{2+} as a charge compensator to get tetravalent Cr. Charge compensating ions in other materials have been shown to affect the optical spectra.[15] YAG also offers a large variety of site symmetries. Y^{3+} ions are dodecahedrally coordinated, 40% of the Al^{3+} ions are octahedrally coordinated, and the other 60% are tetrahedrally coordinated.[16] We can therefore expect to find Cr in different site symmetries as well as in multiple-valence states.

A further difference between Cr^{4+}-doped YAG and other Cr^{4+}-doped materials is the relative difference between the visible and the NIR absorption strength. Most of the Cr^{4+}-doped systems show a visible absorption that is about an order of magnitude stronger than the NIR absorption.[11,13] The strong visible absorption has been assigned to a transition into the ${}^3T_1$ and the NIR absorp-

0163-1829/94/49(22)/15505(9)/$06.00

tion has been assigned to a transition into the $^3T_2$. In Cr:YAG the visible and NIR absorption strength are of the same order of magnitude.

Saturation experiments, described in Ref. 17, have been explained by assuming that the transition into the strong NIR absorption band is polarized along one axis. This is in contrast to the earlier interpretation[18] of this absorption band to be due to the $^3B_1(^3A_2)\Longrightarrow{}^3E(^3T_2)$ transition, since this one would be allowed in two polarizations. Attempts to fit the saturation data with this symmetry were not successful and lead us to a more detailed investigation, resulting in a new assignment of the energy levels in Cr^{4+}:YAG. The results from Ref. 17 together with the here presented data suggest that the strong NIR absorption in Cr:YAG is due to a transition into the lower symmetry component of the $^3T_1$, making the relative strength of the absorption bands in Cr:YAG comparable to other Cr-doped systems.

After presenting some experimental details we give an overview of the basic spectroscopic features in absorption, emission, and excitation. We then discuss the lifetime of the NIR emission and fit its temperature dependence to a model that yields information about radiative-nonradiative ratios and therefore quantum efficiencies. After that, we present results regarding the polarization of some of the observed transitions and introduce a model that can explain our data.

II. EXPERIMENT

The samples of Cr-doped YAG were either co-doped with Ca or Mg (0.2% Cr and 0.1% Ca/Mg molar). Shestakov and Gapontsev of the Russian Academy of Sciences and Kokta of Union Carbide supplied us with the samples. The Russian samples were grown along one of the crystallographic axes and the one from Union Carbide along the [111] axis. The samples were cut perpendicular to their respective growth direction. The spectra of all the samples are identical, no further distinction is therefore made.

The absorption spectra were taken using a tungsten lamp as a light source, an Aries FF500 monochromator to analyze the spectra, and a InGaAs diode to detect the spectra in the NIR, or a Varian VMP 159A photomultiplier to detect the spectra in the visible region. The reference spectrum was taken while the sample was removed from the pathway of the light.

The excitation sources for the fluorescence and excitation spectra were a Q-switched Nd:YAG laser, a dye-laser pumped by the Q-switched, frequency-doubled Nd:YAG laser, a color center laser pumped by the Q-switched Nd:YAG laser, and the Raman shifted output of the dye laser, respectively. The spectra are corrected for excitation intensity variations and detector response. The fluorescence was dispersed by the Aries FF500 monochromator and detected using the InGaAs diode. The same setup has been used to measure the emission lifetimes. For the variation of temperature, a helium closed-cycle refrigerator has been used. For the uniaxial stress experiments a stress device was mounted on the head of the refrigerator. The stress device was accessible through one of the refrigerator windows, so that the amount of pressure could be externally changed.

III. RESULTS AND DISCUSSION

A. Absorption and emission features

Even though the majority of the chromium is octahedrally coordinated Cr^{3+}, the optical spectra of Cr, Ca:YAG is dominated by tetrahedrally coordinated Cr^{4+}. This behavior is due to the lack of inversion symmetry for the tetrahedral site, which allows the mixing of p-wave functions to the d orbitals resulting in an increased oscillator strength. However, one has to keep in mind that all these transitions are parity forbidden in the free ion because they are $3d^2$ innerconfigurational transitions. This selection rule is weakened by the influence of perturbations like the crystal field, which causes an increase in oscillator strength. The transitions do not suddenly become allowed but instead the probability for the transitions increases with the perturbation. If one transition is already more allowed than another one, the same perturbation would increase the probability for both transitions. However, the one that was already more allowed without the perturbation is expected to be still more allowed under the influence of the perturbation.

The ground-state absorption cross section, σ_a, of the Cr,Ca:YAG sample was determined from saturation experiments which are discussed in more detail in Ref. 17. These measurements yielded a cross section of $\sigma_a=5.7\times10^{-18}$ cm^2 at $\lambda=1064$ nm, which is 2–3 orders of magnitude larger than the typical absorption cross section of Cr^{3+} in garnets.[19] There is likely an order of magnitude more Cr^{3+} present in these crystals, but this is not evident from the absorption spectrum. One of the Cr,Ca:YAG crystals (supplied by Kokta) has been used to calculate the percentage of chromium that is incorporated as tetrahedrally coordinated Cr^{4+}. The ground-state absorption coefficient of this crystal was $\alpha=2.6$ cm^{-1} at a wavelength $\lambda=1064$ nm. Using the above-mentioned absorption cross section, the number of Cr^{4+} ions per cubic centimeter was calculated to be $N=4.6\times10^{17}$ cm^{-3}. This gives a Cr^{4+} concentration of $c=0.004\%$. With a total Cr concentration of 0.2 mol% ($N=2.3\times10^{19}$ cm^{-3}) one finds that only 2% of the chromium is tetrahedrally coordinated Cr^{4+}.

The 10-K absorption spectrum of the title compound is shown in Fig. 1. The spectrum shows a broad absorption band in the NIR centered at about 1000 nm and an absorption band in the visible wavelength region between 600 and 700 nm which shows a double structure. The NIR absorption band shows two major peaks at the low-energy side separated by some 300 cm^{-1}. All of these bands have been shown to belong to the NIR emission center.[12] A higher sensitivity scan in the NIR shows that the absorption actually extends down to 1280 nm. In this region some fine structure can be observed, enlarged in the inset of Fig. 1. Two small peaks, visible at about 1280 nm, have been identified as zero-phonon lines.[12] The two peaks are caused by an excited-state splitting and are interpreted as being due to the $^3B_1(^3A_2)\Longrightarrow{}^3B_2(^3T_2)$ tran-

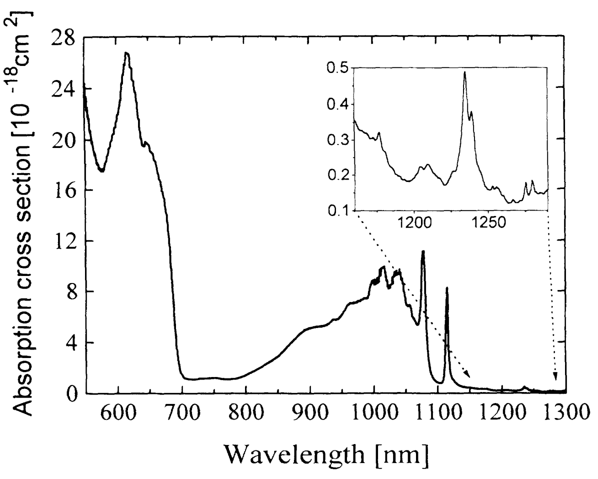

FIG. 1. 10-K absorption spectrum of Cr^{4+}:YAG. The absorption band between 600 and 700 nm has been assigned to the ${}^3B_1 \Longrightarrow {}^3E({}^3T_1)$ transition and the band centered at about 1000 nm has been assigned to the ${}^3B_1 \Longrightarrow {}^3A_2({}^3T_1)$ transition. The inset shows an enlargement of the lowest-energy absorption. The two peaks at around 1280 and 1275 nm are zero-phonon lines of the metastable emitting state. These peaks can also be seen in emission and are the result of a 30-cm^{-1} excited-state splitting.

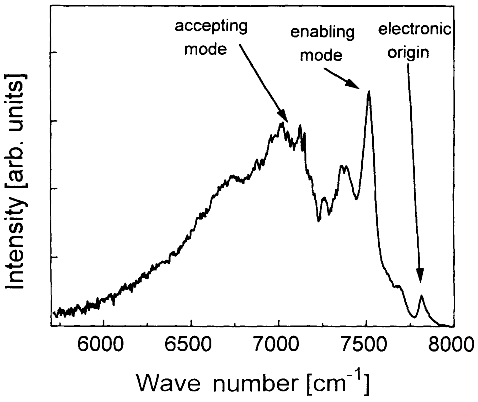

FIG. 2. 10-K emission spectrum of Cr^{4+}:YAG. The spectrum is corrected for the line shape, so that it could be used to determine the Huang-Rhys parameter. The actual zero-phonon line at 1280 nm (7812 cm^{-1}) shows only one peak because the second state is not populated. The peak at 1330 nm (7518 cm^{-1}) is interpreted as an enabling mode which makes the transition electric dipole allowed.

sition which is only allowed as a magnetic dipole transition. The double peak at about 1235 nm is interpreted as a 258-cm^{-1} enabling mode that makes the transition partly electric dipole allowed.

So far the interpretation has been that the strong NIR absorption centered at around 1000 nm is due to the ${}^3B_1({}^3A_2) \Longrightarrow {}^3E({}^3T_2)$ transition and the 600–700-nm band due to the ${}^3B_1({}^3A_2) \Longrightarrow {}^3T_1$ transition of tetrahedrally coordinated Cr^{4+}, respectively. In this work we present a different assignment. Both the strong visible and the strong NIR absorption band are assigned to transitions into the components of the ${}^3T_1$ parent state, i.e., the bands are due to the ${}^3B_1({}^3A_2) \Longrightarrow {}^3E({}^3T_1)$ and the ${}^3B_1({}^3A_2) \Longrightarrow {}^3A_2({}^3T_2)$ transition, respectively. The crystal-field splitting must then be some 5000 cm^{-1} which is of the same order of magnitude as in Mn^{5+} samples.[20] This assignment is the only possibility to explain the polarization behavior of these transitions. Also, the relative strength of the absorption bands would be comparable to other Cr^{4+} systems.

Figure 2 shows the NIR emission at 10 K. The emission starts at 1280 nm (7812 cm^{-1}) with the zero-phonon line and shows a maximum peak at 1330 nm (7518 cm^{-1}) which is interpreted as a 294-cm^{-1} enabling mode that makes the otherwise magnetic dipole transition electric dipole allowed. The vibronic sideband extends down to about 1670 nm (6000 cm^{-1}). The energy difference between the zero-phonon line and the peak at 1330 nm is about the same as the energy difference between the two major peaks in absorption at 1077 nm (9285 cm^{-1}) and 1114 nm (8977 cm^{-1}). It was therefore first believed that the peaks in absorption and emission were mirror images and it was expected to find the electronic origin somewhere in the middle at about 1190 nm.[18] Later it was found that the peak at 1280 nm is the actual zero-phonon line.[12] We show later that the peak at about 1405 nm (7117 cm^{-1}), in Fig. 2, is the one-phonon sideband built on the enabling mode at 1330 nm. The emission spectrum in Fig. 2 is corrected regarding the line shape.[21] We used this spectrum to determine the intensity ratio between the zero-phonon line (here a false origin) and the total intensity to calculate the Huang-Rhys parameter S.[22] From the ratio we get $S = 0.9$. We use this value later to fit the lifetime data. The peak at around 7350 cm^{-1}, in Fig. 2, could be another phonon of about 161 cm^{-1} which has been observed in Raman experiments.[23]

B. Lifetime

The luminescence lifetime of Cr:YAG has been measured at various temperatures and wavelengths using 1064-nm light for excitation. The decays are single exponential and independent of wavelength.

The observed lifetimes at 10 and 300 K are 30.6 and 3.5 μs, respectively. The lifetime decreases right from low temperatures on, i.e., there is no "flat region." This fact indicates that there is already a nonradiative contribution to the decay rate at low temperatures, resulting in a quantum efficiency that is less than 100%. The temperature-dependent integrated emission intensity follows the lifetime curve for low temperatures. For higher temperatures the emission intensity deviates from the lifetime data, suggesting that the radiative decay rate is temperature dependent. For certain excitation wavelengths, it is possible to excite optical centers that emit light at different wavelengths and that have different lifetimes.[24]

The temperature dependence of the decay rate (inverse lifetime) and the temperature dependence of the radiative rate (product of integrated intensity and inverse lifetime) are shown in Fig. 3. The latter curve is used to determine

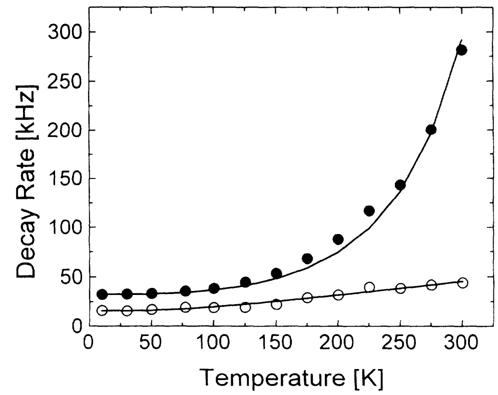

FIG. 3. Temperature-dependent luminescence decay rate (solid circles) of Cr^{4+}:YAG. The missing "flat region" at low temperatures indicates that nonradiative contributions play an important role for the decay even at lowest temperatures. The straight line is a fit using the parameters mentioned in the text. The open circles show the radiative decay. The straight line is a fit using Eq. (3).

the energy of the enabling mode that induces the radiative decay. Both the radiative and the nonradiative rate increase with temperature.

The measured temperature-dependent decay rate $W_m(T)$ (inverse luminescence lifetime, τ_0^{-1}) was fitted using the following equation:

$$W_m(T) = W_r(T) + W_{\mathrm{nr}}(T) , \tag{1}$$

where $W_r(T)$ and $W_{\mathrm{nr}}(T)$ are the temperature-dependent radiative and the temperature-dependent nonradiative decay rates, respectively. Because this model contains six fit parameters, as many of these parameters as possible have to be determined from other experiments. As mentioned earlier, the emission spectrum was used to determine the Huang-Rhys parameter, S, and the initial value of the accepting mode, $\hbar\omega_{\mathrm{accept}}$. The integrated area of the lowest absorption band can be used to calculate the radiative lifetime, and the radiative rate $W_r(0)$ can then be expressed by[25]

$$W_r(0) = \frac{1}{\tau_0} = \frac{8\pi}{\lambda_0^2}\frac{g_1}{g_2} n^2 \int \sigma(\nu) d\nu , \tag{2}$$

where λ_0 is the wavelength of the transition, g_1 and g_2 are the degeneracies of the ground and excited states, n is the index of refraction, and $\sigma(\nu)$ is the absorption cross section as a function of frequency. The absorption cross section at 1064 nm was measured as described in Ref. 17, and used to calculate the cross section for the whole NIR absorption. Using Eq. (2) the radiative lifetime is calculated to be around 85±30 μs. This value (or better its inverse) is used as the initial parameter for $W_r(0)$ in the modeling of the lifetime data. The temperature dependence of the integrated intensity of the NIR emission, shown in Fig. 3, was measured to determine phonon-induced contributions to the radiative rate. Any temperature-dependent radiative contribution to the lifetime will be also indirectly observed by changes of the oscillator strength.

The temperature dependence of the radiative decay rate can be expressed as[26]

$$W_r(T) = W_r(0) \cdot \coth \left[\frac{\hbar\omega_{\mathrm{enab}}}{2kT} \right] , \tag{3}$$

where $W_r(0) = \tau_0^{-1}$ is the radiative decay rate at $T=0$ K, $\hbar\omega_{\mathrm{enab}}$ is a weighted average of enabling modes, and k is the Boltzmann constant. The average energy for the weighted enabling mode from three measurements of the temperature-dependent integrated emission intensity has been determined to be $\hbar\omega_{\mathrm{enable}} = 167 \pm 44$ cm^{-1}.

Because of the small Huang-Rhys parameter, the weak electron-phonon coupling limit is assumed to be valid. The nonradiative decay can therefore be described through multiphonon emission. The expression for the nonradiative decay rate can be written as[26]

$$W_{\mathrm{nr}}(T) = W_{\mathrm{nr}}(0) \cdot e^{-2nS} p! S^{-p} \left[\frac{n+1}{n} \right]^{p/2} \cdot I_p \{ 2S [n(n+1)]^{1/2} \} , \tag{4}$$

where $W_{\mathrm{nr}}(0)$ is the nonradiative contribution at $T=0$ K, $S=0.9$ is the above-mentioned Huang-Rhys parameter, p is the number of phonons involved in the emission, $n = [\exp(\hbar\omega_{\mathrm{accept}}/kT) - 1]^{-1}$ is the Bose-Einstein occupancy factor for the accepting modes $\hbar\omega_{\mathrm{accept}}$, and I_p is the modified Bessel function. The energy of the accepting mode, located around 7100 cm^{-1} in the spectrum in Fig. 2, is determined to be approximately 400 cm^{-1}. The fit of the decay rate was started with the fixed values of $S=0.9$ and $\hbar\omega_{\mathrm{enab}} = 167$ cm^{-1}. $W_r(0) = \frac{1}{85}$ $\mu\mathrm{s} = 11\,765$ s^{-1}, $W_{\mathrm{nr}}(0) = W_m(0) - W_r(0)$, and $\hbar\omega_{\mathrm{accept}} = 400$ cm^{-1} have been used as initial values for the remaining fit parameters. The least-squares fit for the data is shown in Fig. 6 and the full set of parameters is listed in Table I.

Using these data the quantum efficiency, η, is calculated to be 49% at 10 K and 15% at 300 K, which is much lower than the typical quantum efficiency of laser materials like Ti:sapphire (60%) (Ref. 27) or other Cr^{3+}-doped garnets (Cr:GSGG, 91%).[28]

The room-temperature value of 15% has been used to calculate the emission cross section using McCumber's

TABLE I. Radiative and nonradiative parameters for Cr^{4+}:YAG.

Huang-Rhys parameter	S	0.9
Radiative rate at $T=0$ K	$W_r(0)$	16030 s^{-1}
Radiative lifetime at $T=0$ K	$\tau_r(0)$	62.4 μs
Nonradiative rate at $T=0$ K	W_{nr} (0)	16650 s^{-1}
Number of phonons	p	19
Enabling mode	$\hbar\omega_{\mathrm{enab}}$	167 cm^{-1}
Accepting mode	$\hbar\omega_{\mathrm{accept}}$	400.7 cm^{-1}

theory[27,29]

$$\sigma_{\mathrm{em}}=\frac{1}{4\pi}\sqrt{\ln 2/\pi}\,\frac{\lambda_0^4}{\Delta\lambda}\,\frac{n^2}{c\tau_r}\,\eta\ , \tag{5}$$

where $\lambda_0=1350$ nm is the emission center wavelength, $\Delta\lambda=250$ nm is the FWHM of the emission, $n=1.82$ is the index of refraction, c is speed of light, and $\tau_r(300\ \mathrm{K})$ = 23.7 μs is the radiative lifetime at room temperature. This equation then yields an emission cross section $\sigma_{\mathrm{em}}=3.5\times10^{-19}$ cm^2 which is of the same order of magnitude as the emission cross section of Ti^{3+} in sapphire. The room-temperature emission cross section of Cr:YAG extends from around 1200 nm to around 1600 nm with the maximum located at 1350 nm.

C. Polarization-dependent emission

Even though YAG is an overall cubic system, the actual site symmetry of the optical center is less than cubic, i.e., we have the case of anisotropic centers in an overall isotropic crystal. So far the site symmetry for Cr^{4+} has been chosen to be D_{2d}.[30] This symmetry can be considered as an elongated cube. The distortion axis (z axis) of this tetrahedral site coincides with a crystallographic axis. We therefore have three classes of sites oriented along the crystallographic axes. By using polarized light it is possible to selectively excite these classes of ions. The result of this excitation is a highly polarized emission.

Figure 4 shows the 10-K emission spectrum when excited with 1064-nm light, propagating along one and polarized along another crystallographic axis. As one can see, the total emission intensity is much stronger when detected parallel to the excitation polarization than when observed perpendicular to it. However, the intensity of the 1280-nm zero-phonon line seems to be affected in the opposite way compared to the sideband intensity.

The same experiments have been performed for excitation into the visible absorption band. In this case the emission polarization is reversed compared to the 1064 nm excitation. Here the total emission intensity is stronger when observed perpendicular to the excitation polarization.

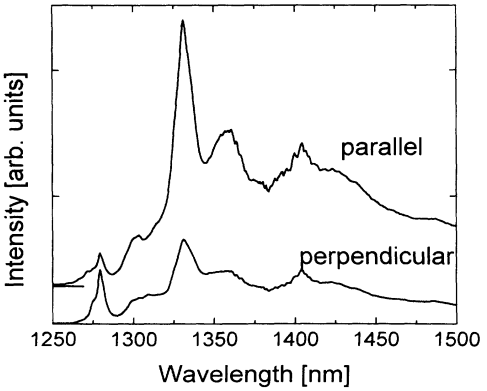

FIG. 4. 10-K emission spectra of Cr^{4+}:YAG. The sample was excited with 1064-nm light polarized along one of the crystallographic axes. The emission was monitored for light polarized parallel and perpendicular to the excitation light polarization. One can clearly see the anisotropy of the enabling mode.

This effect can be explained if one assumes that the transition into the 1000 nm absorption band is electric dipole allowed in one direction parallel to the excitation light polarization and that the transition in the visible region is allowed in two directions perpendicular to the excitation light polarization. This selection rule would cause the excitation of different classes of ions and could then explain the different polarization behavior.

D. Piezospectroscopy

1. *Absorption*

Uniaxial stress experiments have been performed in order to lift the orientational degeneracy in Cr:YAG, i.e., the pressure is used to create a distinctive axis in the otherwise cubic crystal. It is then possible to investigate the optical properties of the Cr^{4+} site using light polarized parallel and perpendicular to the applied pressure. In the following the direction of applied pressure will be denoted as **P**. Using the elastic compliance data[31] and the symmetry for the strain tensor,[32] one finds that YAG shows a contraction in all directions for uniaxial pressure along one of the crystallographic axes. The contraction parallel to the pressure is four times as large as the perpendicular contraction. Since the site symmetry is D_{2d}, in a first approximation uniaxial pressure along one of the crystallographic axes does not change the symmetry, but only the degree of distortion. The main effect of applying uniaxial pressure is therefore the lifting of the orientational and not electronic degeneracy. Uniaxial pressure along (111) leads to a uniform contraction of the YAG crystal.

The investigation of the absorption under uniaxial pressure has been focused on the NIR absorption band in the region between 1000 and 1150 nm. No absorption measurements on the energy level at 1280 nm were possible since the optical path length in the crystal was too short to detect any absorption in this region. The main interest is therefore focused on the two sharp absorption lines at 1077 nm (line A) and at 1114 nm (line B). The effect of uniaxial pressure along different crystallographic directions on the absorption spectra of Cr:YAG is shown in Fig. 5. Since the sites are oriented along the crystallographic axes no splitting due to orientational degeneracy is expected for pressure along (111). This is confirmed by the experiments.

When pressure is applied along one of the crystallographic axes, for example, along (001) in Fig. 5, the orientational degeneracy between the three classes of sites (A,B,C) is lifted. Sites oriented parallel to **P** and sites oriented perpendicular to **P** can then be distinguished. For Cr:YAG these are site C (001), and sites A (100) and B (010), respectively.

Pressure-dependent absorption experiments were thus performed to get additional support for the assignment of the NIR absorption to the ${}^3B_1({}^3A_2)\Longrightarrow{}^3A_2({}^3T_1)$ transition. If this absorption band was due to the ${}^3B_1({}^3A_2)\Longrightarrow{}^3E({}^3T_2)$ transition, it should be allowed for x and y polarization, while if it was due to the

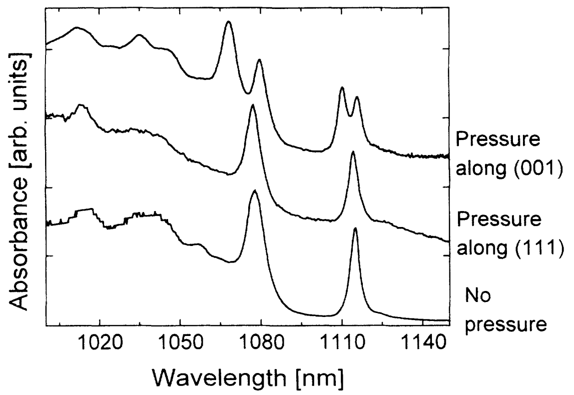

FIG. 5. 10-K absorption spectra of Cr:YAG for pressure along (001) (top), pressure along (111) (middle), and zero pressure (bottom). The applied pressure was around 9 kbar.

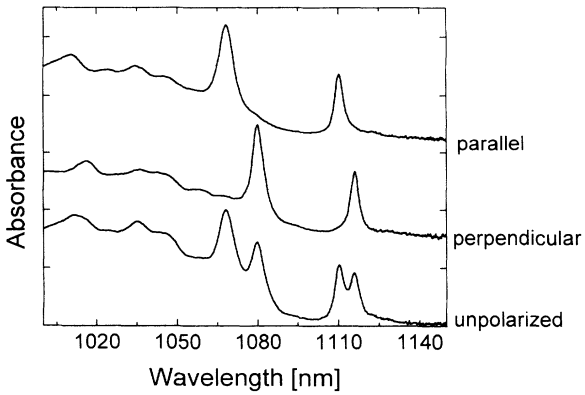

FIG. 6. 10-K absorption spectra of Cr:YAG under pressure (9 kbar). The lower trace shows the unpolarized spectrum. The splitting is caused by lifting the orientational degeneracy. The two upper traces show clearly the strong polarization of the orthogonally oriented sites.

$^3B_1(^3A_2) \Longrightarrow {}^3A_2(^3T_1)$ transition, it should only be allowed in z polarization. Assuming that the band is due to the $^3B_1(^3A_2) \Longrightarrow {}^3E(^3T_2)$ transition, as proposed by Kück *et al.*,[18] one would expect to see the following scenario using polarized light. With light polarized along (001), i.e., parallel to **P**, site A (100) and site B (010) should show absorption but not site C (001). Since sites A and B are degenerate, i.e., these sites are equally affected by the pressure, no orientational splitting is expected. Using light polarized perpendicular to **P**, i.e., either parallel to (100) or (010), again the sites oriented perpendicular to the incident light polarization should show absorption. These would be site C (001), and either site A or B, depending on the incident light polarization. Since the orientational degeneracy between site C and sites A and B is now lifted, it is expected to see a splitting in the absorption spectrum, with absorption peaks belonging to site C and either site A or site B.

If the NIR absorption belonged to the $^3B_1(^3A_2) \Longrightarrow {}^3A_2(^3T_1)$ transition as proposed here, a different feature would be expected because this transition is allowed in z polarization only. Using light polarized parallel to the applied stress one expects to see the absorption from site C which is oriented along (001), but no absorption from site A or B. Using light polarized perpendicular to **P** one should see absorption only from site A or B. Since the orientational degeneracy is lifted, one expects these spectra to be complementary, i.e., only one set of lines should be seen for each polarization direction.

The experimental data are in good agreement with the latter case, as shown in Fig. 6. The bottom trace shows the 10-K absorption spectrum of Cr:YAG under uniaxial pressure along a crystallographic axis using unpolarized light. The middle and the top traces show the same absorption spectra using polarized light. For the unpolarized light both absorption peaks (line A and line B) show a splitting. Using light polarized either parallel or perpendicular to **P** only one peak can be seen in line A and line B, i.e., the spectra are complementary. These findings support the above assignment of this absorption to the $^3B_1(^3A_2) \Longrightarrow {}^3A_2(^3T_1)$ transition.

Lines A and B show the same polarization dependence (polarized along the z direction) and it is therefore likely that both belong to the same transition. However, the interpretation of these two lines is not easy. They cannot be due to a spin-orbit splitting of the $^3A_2$ because this interaction would split the $^3A_2$ into states of Γ_1 and a Γ_5 symmetry and the transition from the ground state into these states would be allowed in different polarizations. Another possibility would be to consider line B as an electronic origin of the $^3A_2$ and line A as a 308-cm^{-1} vibrational mode of even parity.

These lines shift under pressure with the following rates. For light polarized parallel to **P** line A shifts with 9.2 cm^{-1}/kbar to higher energies and line B with 3.8 cm^{-1}/kbar to higher energies. For light polarized perpendicular to **P**, line A shifts with 2.6 cm^{-1}/kbar and line B with 1.7 cm^{-1}/kbar both to smaller energies. The direction of the shift with pressure can easily be understood if one considers the shape of the tetrahedron and the pressure direction. Site C (001) is initially elongated along the direction of **P**. With increasing pressure the elongation of the tetrahedron decreases, i.e., the tetrahedron becomes more cubic and therefore reduces the orbital splitting of the $^3T_1$ state, i.e., the ^3E and the $^3A_2$ states are moving closer together, with the $^3A_2$ state shifting to higher energies. At the same time, the cubic crystal-field component increases. Both effects cause a shift to higher energy. For sites A and B, the D_{2d} distortion is increased, i.e., the splitting of the $^3T_1$ state increases, so that the $^3A_2$ state shifts to lower energies. However, the resulting shift in this case is smaller because the cubic component is still shifted to higher energies and compensates for part of the shift to lower energies.

2. Emission

As seen before, application of uniaxial pressure along the (001) axis leads to a lifting of the orientational degeneracy. Since the excitation with 1064-nm light is into a

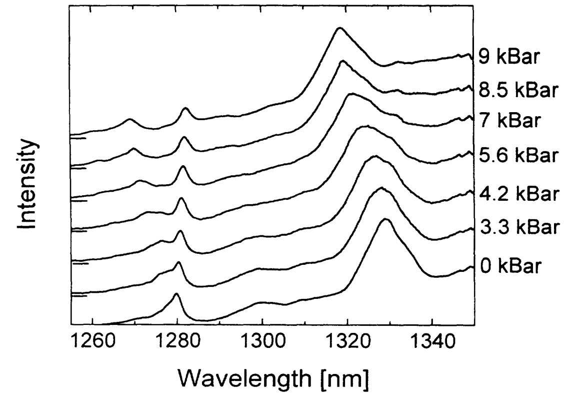

FIG. 7. 10-K emission of Cr^{4+}:YAG for increasing pressure (bottom to top). The zero-phonon line at 1280 nm splits into two components which are due to the sites oriented parallel and perpendicular to the applied pressure.

vibronic sideband, as shown in Fig. 1, both classes of ions, those oriented parallel and perpendicular to **P**, are excited. Both classes also emit light in their respective zero-phonon line. The 10-K emission spectrum of Cr:YAG for excitation with 1064-nm light polarized parallel to the (001) direction is shown in Fig. 7.

The orientational degeneracy is lifted with increasing pressure, and emission from both classes of ions appears. The lower-energy zero-phonon line shifts to smaller energies while the less intense, high-energy zero-phonon line shifts to higher energies. Also, with increasing temperature both zero-phonon lines show a hotband. The polarization-dependent zero-phonon line emission at 65 K is shown in Fig. 8.

As discussed for the pressure-dependent absorption experiments, for light polarized parallel to **P** only the higher-energy peaks are visible. In emission, the higher-energy peak is stronger when observed perpendicular to **P**. This shows that the transition from the emitting state is polarized perpendicular to z, i.e., along x and/or y. This observation confirms that the metastable state is indeed the $^3B_2$. The hotband emission shows the same polarization dependence as the coldband.

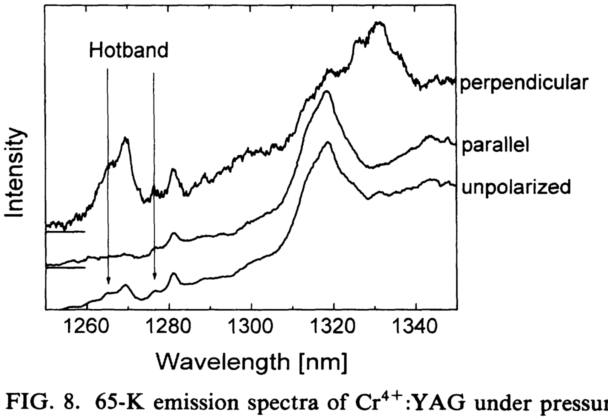

FIG. 8. 65-K emission spectra of Cr^{4+}:YAG under pressure when excited with 1064-nm light polarized parallel to the applied pressure. The bottom trace shows the unpolarized emission, the trace in the middle the parallel to the applied pressure polarized emission, and the top trace the perpendicular to the applied pressure polarized emission. The hotband of the zero-phonon line can be seen as a shoulder on the high-energy side. As shown before, the sideband intensity is much lower when the observed emission is polarized perpendicular to the excitation polarization.

E. Energy-level assignment

As shown in Fig. 9, in an ideal tetrahedral site (T_d symmetry), the lowest free-ion level of the Cr^{4+} ion ^{3}F splits into three components,

$$^3\mathrm{F} \Longrightarrow {}^3A_2 + {}^3T_2 + {}^3T_1 \ ,$$

with the energy of these levels being $^3A_2 < {}^3T_2 < {}^3T_1$. Group theory[33] predicts that, with the $^3A_2$ level as the ground state the $^3A_2 \Longleftrightarrow {}^3T_1$ transition would be electric dipole allowed while the $^3A_2 \Longleftrightarrow {}^3T_2$ transition would only be magnetic dipole allowed in all polarizations and should therefore be orders of magnitude less intense than the $^3A_2 \Longleftrightarrow {}^3T_1$ transition.

Lowering the symmetry of the site to D_{2d}, i.e., stretching the tetrahedrons along the crystallographic axes, changes the ground state and results in an orbital splitting of the excited states. In D_{2d} symmetry, the ground state $^3A_2$ becomes $^3B_1$, the $^3T_2$ splits into $^3B_2$ and ^3E and the $^3T_1$ splits into $^3A_2$ and ^3E. The transitions from the ground state into the ^3E levels are electric dipole allowed in x and y polarizations. However, it is expected that the transition into the $^3E(^3T_1)$ state is stronger than that into the $^3E(^3T_2)$ state because the transition into the parent state in a T_d symmetry was already electric dipole allowed for the former and only magnetic dipole allowed for the latter. The $^3B_1 \Longleftrightarrow {}^3A_2(^3T_1)$ transition is electric dipole allowed in z polarization while the $^3B_1 \Longleftrightarrow {}^3B_2(^3T_2)$ transition is only magnetic dipole allowed (R_z). These energy levels, and the allowed electric and magnetic dipole transitions, are shown in Fig. 10. Also shown are

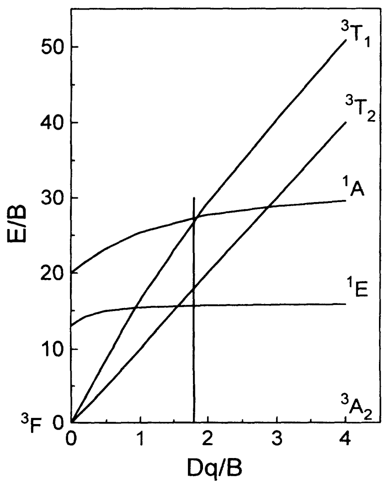

FIG. 9. Tanabe-Sugano diagram for tetrahedrally coordinated Cr^{4+}:YAG. The vertical line indicates the appropriate crystal-field strength of $Dq/B = 1.78$ for Cr:YAG.

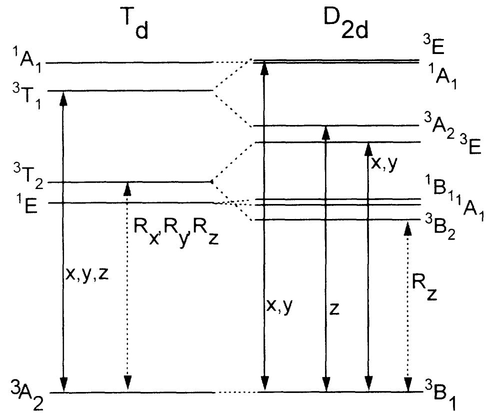

FIG. 10. Energy-level diagram for tetrahedrally coordinated Cr^{4+} in T_d and D_{2d} symmetry. Electric dipole allowed transitions are marked by straight lines while magnetic dipole transitions are marked by dotted lines.

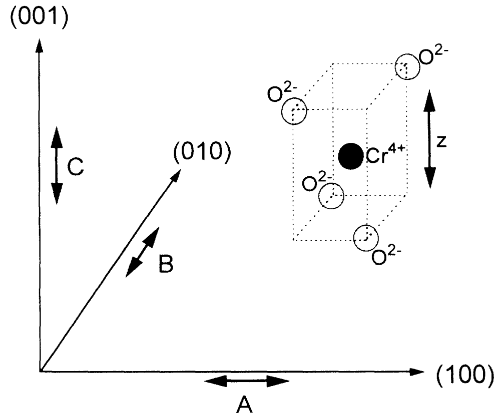

FIG. 11. Orientation of the z axis of the sites A, B, and C with respect to the crystallographic axes.

two additional energy levels, ^1E and $^1A_1$, which result from the ^1D and ^1G free-ion states. It is very difficult to find absorption into these states since the transitions are forbidden. However, a tentative assignment based on crystal-field calculations will be given later.

The visible absorption band between 600 and 700 nm is assigned to the $^3B_1(^3A_2) \Longrightarrow {}^3E(^3T_1)$ transition, and the strong NIR absorption band centered at around 1000 nm to the $^3B_1(^3A_2) \Longrightarrow {}^3A_2(^3T_1)$ transition. The shoulder on the low-energy side of the visible absorption band might be due to a lower symmetry (D_2 component) orbital splitting of the $^3E(^3T_1)$ excited state. The weak NIR absorption at 1280 nm is due to the $^3B_1(^3A_2) \Longrightarrow {}^3B_2(^3T_2)$ transition, while an absorption at 1206 and 1210 nm is tentatively assigned to the $^3B_1(^3A_2) \Longrightarrow {}^1E$ transition. It was not possible to clearly identify the location of the $^3B_1(^3A_2) \Longrightarrow {}^3E(^3T_2)$ transition. This absorption might be hidden under the strong NIR absorption band and some justification for this is given later. The energy level assignments made here satisfactorily explain the experimental data.

If the three classes of sites that are oriented along the crystallographic axes are labeled *A* (100), *B* (010), and *C* (001), then their respective *z* axes (or elongation axes) are those parallel to the respective crystallographic axes of the host, as shown in Fig. 11.

For light (1064 nm) propagating along (100) and polarized parallel to (001), the absorption occurs through ions at site *C*. Emission along (010) can be detected for polarizations parallel to (001) and (100), parallel and perpendicular to the excitation polarization, respectively. After relaxation to the lowest excited state ($^3B_2$), site-*C* ions emit magnetic dipole radiation (electric component perpendicular to its *z* axis) and the zero-phonon line emission is thus polarized along (010) or (100). In the ideal case, the zero-phonon line emission should therefore only be polarized perpendicular to the excitation polarization. However, the experimental data for the 1064-nm excitation also show a parallel component which is probably due to transition rules that are not totally strict. Nevertheless, the perpendicular emission polarization is clearly stronger than the parallel one, see Fig. 4.

Using visible excitation light (600–700 nm) in an identical geometry, site *A* and *B* ions are now excited. The ions in both sites have a zero-phonon line emission that is polarized perpendicular to their respective *z* axes. Site *A* emits light polarized along (010) and (001) and site *B* emits light polarized along (100) and (001). In this case the intensity of parallel polarized light (001) is larger than the perpendicular one. This is confirmed by the experiments.

The above-mentioned energy level assignment clearly identifies the main features of the zero-phonon emission intensities. The sideband intensity however, shows exactly the opposite behavior. Raman experiments have shown the coupling of e_g modes,[23] which induce an anisotropy, making the transition electric dipole allowed and thus satisfactorily explains the stronger sideband intensities and the polarization behavior.

Crystal-field calculations based on a scheme developed by Tanabe and Sugano[34] have been performed. A good description is found in Henderson and Imbusch.[22] In this scheme, the variation of energy with the Racah parameter is as displayed in Fig. 9.

Using the approximate matrix elements, the following crystal-field parameters have been fitted: $Dq = 915\ \mathrm{cm}^{-1}$, $B = 515\ \mathrm{cm}^{-1}$, and $C = 4.2B$, resulting in $Dq/B = 1.78$. The transition into the excited state $^3E(^3T_2)$ would then be located at 1018 nm, overlapped by the strong NIR absorption and the ^1E at 1208 nm. The strong visible absorption band would overlap the excited state ^1A, which would be located at 592 nm. This shows also that Cr:YAG is indeed a high-field system as indicated in Fig. 9 by the vertical line. In sum, the above energy assignment describes the experimental data and indicates that only the strong orbital splitting of the $^3T_2$ makes Cr:YAG look like a low-field system.

IV. CONCLUSION

In this work we presented a detailed analysis of the static and dynamic spectroscopic properties of

Cr^{4+}:YAG. Cr^{4+} is shown to occupy tetrahedral sites (D_{2d} symmetry). The first excited state is the $^3B_2$ component of the $^3T_2$ state. The transition between the ground state and this first excited state is only allowed as a magnetic dipole transition. Coupling to a 294-cm^{-1} enabling mode makes the transition electric dipole allowed. The ^3E component of the $^3T_2$ state is probably hidden under the strong absorption band centered at around 1000 nm. We assign this strong absorption band to the transition into the $^3A_2(^3T_1)$ state because of its polarization behavior. This band had earlier been assigned to the transition into the $^3E(^3T_2)$ state. Because of its polarization behavior we assign the absorption band between 600 and 700 nm to the transition into the $^3E(^3T_1)$ component. The evidence for this assignment comes from piezospectroscopic and polarization dependent experiments as well as earlier performed saturation experiments.

The luminescence decay rate has been shown to be due to radiative and nonradiative contributions. Nonradiative contributions seem to play an important role even at lowest temperatures. The quantum efficiency η at 10 and 300 K has been determined to be 49 and 15%, respectively.

ACKNOWLEDGMENTS

We are grateful to R. S. Meltzer for helpful discussions. This work was partly supported by DARPA Contract No. N00014-90-4088 and by NSF Grant No. DMR-9117077. One of the authors (W.J.) is grateful to the U.S. Army Research Office (Grant No. DAAL03-91-G-0317) and EPSCoR-NSF.

---

[1] V. Petricevic, S. K. Gayen, and R. R. Alfano, Appl. Phys. Lett. **53**, 2590 (1988).

[2] H. R. Verdun, L. M. Thomas, D. M. Andrauskas, and T. McCollum, Appl. Phys. Lett. **53**, 2593 (1988).

[3] N. I. Borodin, V. A. Zhitnyuk, A. G. Okhrimchuk, and A. V. Shestakov, Izv. Akad. Nauk SSSR, Ser. Fiz. **54**, 1500 (1990).

[4] W. Jia, H. Eilers, W. M. Dennis, W. M. Yen, and A. V. Shestakov, in *OSA Proceedings on Advanced Solid State Lasers*, edited by L. L. Chase and A. A. Pinto (Optical Society of America, Washington, DC, 1992), Vol. 13, pp. 31–33.

[5] H. Eilers, W. M. Dennis, W. M. Yen, S. Kück, K. Petermann, G. Huber, and W. Jia, IEEE J. Quantum Electron. **29**, 2508 (1993).

[6] S. Kück, J. Koetke, K. Petermann, U. Pohlmann, and G. Huber, *OSA Proceedings on Advanced Solid State Lasers* (Optical Society of America, Washington, DC, 1993).

[7] J. A. Capobianco, G. Cormier, M. Bettinelli, R. Moncorge, and H. Manaa, J. Lumin. **54**, 1 (1992).

[8] M. Herren, H. U. Güdel, C. Albrecht, and D. Reinen, Chem. Phys. Lett. **183**, 98 (1991).

[9] M. Herren and H. U. Güdel, Inorg. Chem. **31**, 3683 (1992).

[10] W. Jia, H. Liu, S. Jaffe, and W. M. Yen, Phys. Rev. B **43**, 5234 (1991).

[11] U. Hömmerich, H. Eilers, S. M. Jacobsen, W. M. Yen, and W. Jia, J. Lumin. **55**, 293 (1993).

[12] K. R. Hoffman, U. Hömmerich, S. M. Jacobsen, and W. M. Yen, J. Lumin. **52**, 277 (1992).

[13] C. Deka, M. Bass, B. H. T. Chai, and X. X. Zhang, *OSA Proceedings on Advanced Solid State Lasers* (Ref. 4), pp. 47–51.

[14] R. Moncorge, G. Cormier, D. J. Simkin, and J. A. Capobianco, IEEE J. Quantum Electron. **27**, 114 (1991).

[15] A. Brenier, A. Suchocki, C. Pedrini, G. Boulon, and C. Madej, Phys. Rev. B **46**, 3219 (1992).

[16] G. Winkler, *Magnetic Garnets* (Friedr. Vieweg & Sohn, Braunschweig/Wiesbaden, 1981).

[17] H. Eilers, K. R. Hoffman, W. M. Dennis, S. M. Jacobsen, and W. M. Yen, Appl. Phys. Lett. **61**, 2958 (1992).

[18] S. Kück, K. Petermann, and G. Huber, in *OSA Proceedings on Advanced Solid State Lasers*, edited by G. Dube and L. Chase (Optical Society of America, Washington, DC, 1991), Vol. 10, pp. 92–94.

[19] J. Drube, Ph.D. thesis, University of Hamburg, 1987, p. 36.

[20] R. Borromei, L. Oleari, and P. Day, J. Chem. Soc. Faraday Trans. 2 **77**, 1563 (1981).

[21] A. J. Wojtowicz, M. Kazmierczak, A. Lempicki, and R. H. Bartram, J. Opt. Soc. Am. B **6**, 1106 (1989).

[22] B. Henderson and G. F. Imbusch, *Optical Spectroscopy of Inorganic Solids* (Clarendon, Oxford, 1989).

[23] K. Petermann (private communication).

[24] H. Eilers, U. Hömmerich, S. M. Jacobsen, and W. M. Yen, *OSA Proceedings on Advanced Solid State Lasers* (Optical Society of America, Washington, DC, 1993).

[25] B. Di Bartolo, *Optical Interactions in Solids* (Wiley, New York, 1968).

[26] P. S. May and H. U. Güdel, J. Lumin. **46**, 277 (1990).

[27] P. Albers, E. Stark, and G. Huber, J. Opt. Soc. Am. B **3**, 134 (1986).

[28] W. Seelert and E. Strauss, Opt. Lett. **12**, 798 (1987).

[29] D. E. McCumber, Phys. Rev. **134**, A299 (1964).

[30] N. I. Borodin, A. G. Okhrimchuk, and A. V. Shestakov, *OSA Proceedings on Advanced Solid State Lasers* (Ref. 4), pp. 42–46.

[31] A. A. Kaminskii, *Laser Crystals*, Springer Series in Optical Sciences (Springer-Verlag, Berlin, 1981).

[32] T. S. Narasimhamurty, *Photoelastic and Electro-Optic Properties of Crystals* (Plenum, New York, 1981).

[33] B. E. Douglas, *Symmetry in Bonding and Spectra* (Academic, Orlando, 1985).

[34] Y. Tanabe and S. Sugano, J. Phys. Soc. Jpn. **9**, 7543 (1954).

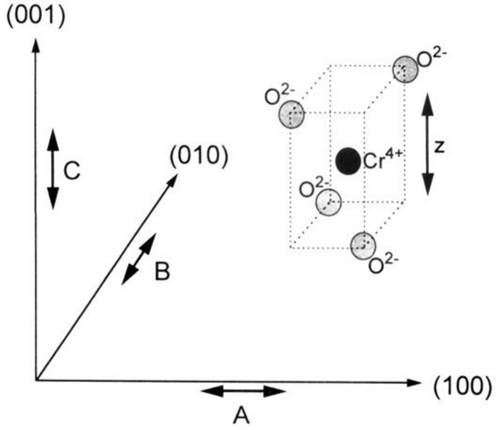

FIG. 11. Orientation of the *z* axis of the sites *A*, *B*, and *C* with respect to the crystallographic axes.